ACS APPLIED MATERIALS & INTERFACES

www.acsami.org

Research Article

Direct Laser Writing of Microscale Metal Oxide Gas Sensors from Liquid Precursors

Alexander C. Castonguay,[¶] Ning Yi,[¶] Bowen Li, Jiang Zhao, Han Li, Yuyan Gao, Nabila N. Nova, Naveen Tiwari, Lauren D. Zarzar,* and Huanyu Cheng*

Cite This: *ACS Appl. Mater. Interfaces* 2022, 14, 28163–28173

Read Online

ACCESS | Metrics & More | Article Recommendations | Supporting Information

ABSTRACT: Fabrication and processing approaches that facilitate the ease of patterning and the integration of nanomaterials into sensor platforms are of significant utility and interest. In this work, we report the use of laser-induced thermal voxels (LITV) to fabricate microscale, planar gas sensors directly from solutions of metal salts. LITV offers a facile platform to directly integrate nanocrystalline metal oxide and mixed metal oxide materials onto heating platforms, with access to a wide variety of compositions and morphologies including many transition metals and noble metals. The unique patterning and synthesis flexibility of LITV enable the fabrication of chemically and spatially tailorable microscale sensing devices. We investigate the sensing performance of a representative set of n-type and p-type LITV-deposited metal oxides and their mixtures (CuO, NiO, CuO/ZnO, and Fe_2O_3/Pt) in response to reducing and oxidizing gases (H_2S, NO_2, NH_3, ethanol, and acetone). These materials show a broad range of sensitivities and notably a strong response of NiO to ethanol and acetone (407 and 301% R/R_0 at 250 °C, respectively), along with a 5- to 20-fold sensitivity enhancement for CuO/ZnO to all gases measured over pure CuO, highlighting the opportunities of LITV for the creation of mixed-material microscale sensors.

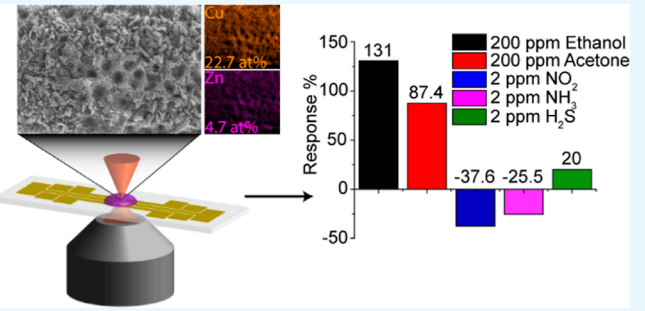

KEYWORDS: *gas sensor, laser direct writing, micropatterning, nanocrystalline, metal oxide, laser synthesis*

1. INTRODUCTION

The detection of gases is of critical importance to various fields, including pollution monitoring, public safety assurance, and personal healthcare.[1−4] Sensing devices are desirably small, lightweight, inexpensive, easy to use, and applicable to various environments and substrates, such as clothing or piping. Metal oxide semiconductors have been widely used for many gas-sensing applications due to their high sensitivity, reversibility, ease of use, and low cost.[5−8] Most metal oxide semiconductor gas sensors function by measuring the change in electrical resistance caused by the adsorption of gas molecules on the metal oxide surface,[9] which can then be correlated to a specific gas concentration using a calibration standard. Metal oxide semiconductor gas sensors typically are equipped with a heater, which is necessary to increase the otherwise sluggish gas adsorption and desorption kinetics that can cause poor sensitivity and slow recovery. In many commercial platforms, such as household carbon monoxide detectors, these heaters are resistive wires that fit into a hollow ceramic tube coated with a nanoparticle slurry of the sensing material. However, this design makes the sensors prohibitively large and unsuitable in cases where microscale or single-millimeter scale device footprints are desired, evidentiating the need for research and development in microheaters and metal oxide semiconductor micropatterning methods. In addition to the challenges associated with miniaturizing the sensor footprint, metal oxide semiconductor sensors tend to have intrinsically poor selectivity. For instance, when using an n-type metal oxide semiconductor, any oxidizing gas that interacts with the oxide surface will increase the measured resistance. In contrast, reducing gases will decrease resistance, making it difficult to distinguish between various gas species and determine the composition of gaseous mixtures. Approaches to address such challenges of miniaturization and selectivity are needed.

Research aimed at enhancing selectivity and sensitivity is primarily focused on synthesizing metal oxide semiconductor nanoparticle structures and compositions with tailored surface functionalization, as well as the formation of mixed materials with heterojunctions.[10,11] Synthetic approaches include sol−precipitation,[10] sol−gel synthesis,[11] hydrothermal synthesis,[12] and mechanical mixing.[13] Nanomaterial morphologies with

Received: February 25, 2022
Accepted: May 30, 2022
Published: June 10, 2022

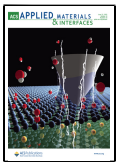

https://doi.org/10.1021/acsami.2c03561
ACS Appl. Mater. Interfaces 2022, 14, 28163−28173

high specific surface areas have been shown to have a drastic impact on gas sensor sensitivity, with many different morphologies reported, including nanoflowers,[14,15] nanotubes,[16] nanospheres,[17] and nanowires.[18,19] When two types of metal oxides contact each other to form a heterojunction (e.g., p−n junction), their inherently different Fermi levels will be equilibrated as the electrons at higher energy levels flow to unoccupied lower energy states through the interface. This Fermi-level equilibration generates a potential energy barrier at the interface. Gas molecules adsorbed at the heterojunction interface can tune the potential barrier and affect the conductivity of the mixed metal oxide gas sensor. This potential energy barrier level at the metal oxides' interface is more sensitive to gas analyte adsorption/desorption, thus often making mixed metal oxides more responsive than the single metal oxides.[20,21] When heterojunctions are formed with oxides that show preferential adsorption or catalytic activity toward specific gas molecules, this can create a selective interface where the response to those specific gas molecules is enhanced significantly.[22] The presence of metal oxide/metal oxide junctions also reportedly gives rise to other types of sensing mechanisms such as the synergistic effect, spill-over effect, and n−p−n response type inversions.[23] Many material combinations and structures of heterojunctions are possible, but no universal theory to explain the enhanced gas-sensing performance of mixed metal oxides yet exists.[24] Thus, further research is necessary to understand how to tailor combinations of metal oxide heterojunctions for specific gas analysis.

Once the desired nanomaterials are synthesized, they must be integrated into a gas-sensing platform. Common metal oxide semiconductor patterning methods for device integration include drop-casting and screen printing.[25] Both methods are simple, inexpensive techniques, but their inherently low resolution makes it difficult to integrate multiple metal oxide semiconductor materials within a microscale footprint. For drop-casting, spreading of the droplet makes it challenging to define the pattern of metal oxides accurately, and weak adhesion between the metal oxide and electrodes can lead to poor electrical contact.[26−28] Screen printing provides improved spatial control using stencils or shadow masks, but the resolution is limited to ∼150 μm, and the process wastes significant amounts of material.[29] To overcome these limitations, some researchers have used microheaters as miniaturized hydrothermal reactors. This method has been used to grow ZnO nanowires, CuO nanospikes, and TiO_2 or SnO_2 nanotubes directly on the microheater, removing the need to integrate the metal oxide with a heat source after material synthesis.[30] Laser-based techniques have also gained interest due to the ease of customization afforded by maskless patterning and opportunities for simultaneous metal oxide nanoparticle synthesis and surface deposition.[31] For instance, laser-induced hydrothermal growth (LIHG), where metal oxide nanowires or nanoparticles are synthesized directly from solution at a laser focus, has been demonstrated for the microscale patterning of ZnO and TiO_2 nanowires[32] as well as various transition-metal oxides.[33] Proof-of-concept optical sensors and capacitors have been fabricated using this technique.[33,34] The spatial control inherent to laser-based synthesis and patterning techniques makes them uniquely suited to address challenges associated with the design and fabrication of microscale, multi-component gas sensors. To our knowledge, the majority of reports using direct laser writing to fabricate gas sensors focus on synthesis of graphene oxide,[35,36] with no reports of direct laser writing of metal oxide gas sensors. Due to these characteristics, the development and application of laser-based techniques for sensor fabrication constitutes a rich and potentially fruitful area of research that remains largely unexplored and could enable significant advances in the design of complex, integrated devices.

This article explores the design and properties of microscale metal oxide semiconductor gas sensors fabricated using the laser-induced thermal voxel (LITV) process, which is a maskless, liquid-based laser writing technique that enables the synthesis and patterning of diverse multi-component oxide nanomaterials directly from solution with sub-10 μm resolution.[37,38] This technique uses a focused laser to induce solvothermal decomposition of precursors in solution, generating nanoparticles that are sintered to the sensor substrate as the laser is scanned. Rinsing and replacing the precursor solution allows for patterning of multiple metal oxide materials on a single substrate. The ease of metal oxide compositional variation combined with high-resolution patterning makes the LITV technique of interest for the fabrication of metal oxide semiconductor gas-sensing devices. The rapid thermal decomposition achieved during LITV, at temperatures greater than 1000 °C,[37] allows for faster laser patterning compared to the slow hydrothermal growth process used in LIHG.[32,33] Thermal decomposition is also less chemically sensitive than hydrothermal growth, giving LITV access to a far wider range of material compositions, including mixed composition, heterostructured materials.[38]

Here, we describe the use of LITV in the creation of single-metal oxide (NiO and CuO), noble-metal-doped metal oxide (Pt-doped Fe_2O_3), and mixed-metal oxide (CuO/ZnO) microscale gas sensors directly on pre-patterned electrodes. We examine the response to various industrially and environmentally relevant oxidizing and reducing gases, including ethanol, acetone, H_2S, NO_2, and NH_3. We find NiO exhibits the largest response to all gases of the single metal oxides tested, with a notable response to volatile organics (407 and 301% response to 200 ppm ethanol and acetone, respectively). CuO exhibits a lower response of 14 and 4% to the same ethanol and acetone concentrations, with negligible response to H_2S, NO_2, or NH_3. Fe_2O_3 suffered from a considerable intrinsic resistance, but we found that doping 4 at. % Pt into the Fe_2O_3 improved its signal quality, resulting in a response of −26.2% to 200 parts-per-million (ppm) ethanol. Notably, we find that the creation of a mixed 5:1 at. % ratio CuO/ZnO material significantly enhances p-type sensitivity toward all gases compared to pure CuO, with an inversion of p-type to n-type character when exposed to NH_3. While this report only explores a small fraction of the possible metal oxide semiconductor gas sensor compositions and morphologies accessible with the LITV technique, these initial findings demonstrate the utility of this laser-based process for gas sensor fabrication. The core innovation is our ability to use laser writing to simultaneously synthesize and pattern numerous mixed metal oxides directly from fluids onto a sensing platform. This combined synthesis and patterning allows us to deposit highly varied materials with microscale precision, streamlining fabrication by eliminating the need to first create a material and then pattern it onto a device. Due to this flexibility, we believe the results from this work have a high potential to enable the patterning of high-density arrays of different sensing materials necessary for microscale, combinatorial gas sensing, as well as enable high-throughput testing of

https://doi.org/10.1021/acsami.2c03561
ACS Appl. Mater. Interfaces 2022, 14, 28163−28173

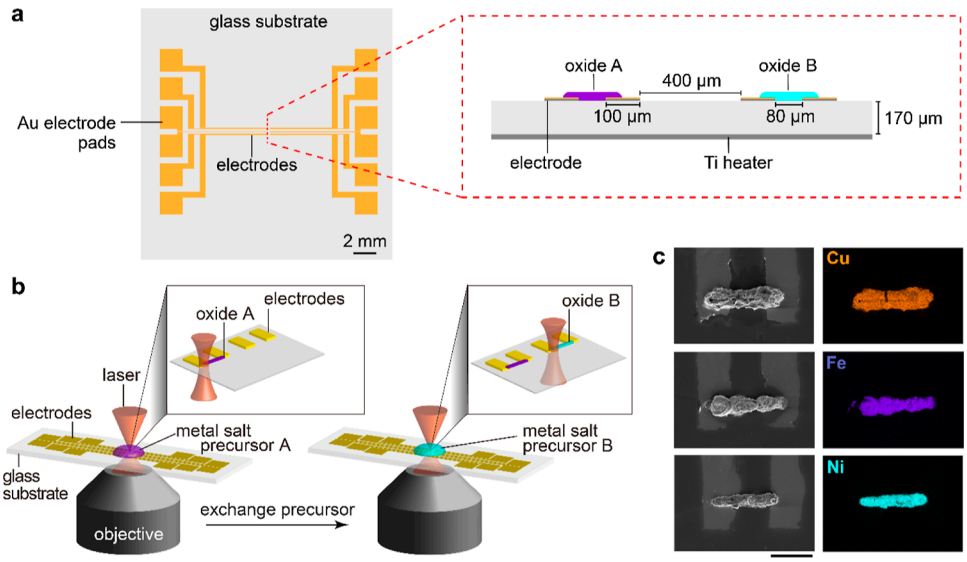

Figure 1. LITV synthesis of metal oxide gas sensors. (a) Macroscopic and cross-sectional (boxed-area) illustration of the sensor, with gold electrodes bridged with metal oxides deposited using LITV and a titanium heater on a glass coverslip substrate (detailed in Figures S1−S3). (b) Generalized schematic of the LITV deposition process. LITV is used to print metal oxide lines from aqueous metal salt solutions directly onto the sensor substrate by scanning the focal point of a 780 nm laser. Metal oxide composition is varied by exchanging the precursor used for deposition, allowing multiple oxides to be precisely patterned on the same sensor device. (c) Scanning electron microscopy (left) and energy dispersive X-ray spectroscopy (right) images show three single-metal oxides bridging their respective electrodes. Energy-dispersive X-ray spectroscopy confirms the presence of three different metal oxides containing Cu, Fe, and Ni. The oxides were confirmed as CuO, NiO, and α-Fe_2O_3 by X-ray diffraction (Figure S4). Scale bar, 100 μm.

novel sensing materials, which is of particular interest to fields such as human health care and precision agriculture.[39−42]

2. RESULTS AND DISCUSSION

2.1. Sensor Fabrication and Material Characterization. To evaluate whether LITV-deposited materials could be suitable for gas sensing, we first sought to synthesize a variety of p-type and n-type oxides. The oxides are expected to provide a resistive sensing response: CuO and NiO as p-type semiconductors and α-Fe_2O_3 as an n-type semiconductor. We fabricated substrates containing six pairs of gold electrodes using electron beam evaporation on glass coverslips (Figure 1a) and then used these as substrates for LITV deposition (Figure 1b). The electrodes themselves served as the optical absorber necessary for initiating LITV deposition. By scanning the focus of a continuous wave 780 nm laser, we printed these different oxides onto the same electrode array (Figure 1c) using aqueous solutions of metal nitrate salts as the fluid precursors (refer to Experimental Methods for details). From X-ray diffraction of annealed samples, we observe deposition of single-phase nanocrystalline oxides of α-Fe_2O_3, CuO, and NiO from aqueous solutions of $Fe(NO_3)_3$, $Cu(NO_3)_2$, and $Ni(NO_3)_2$, respectively (Figure S4). Rietveld refinement of the NiO X-ray diffraction pattern revealed crystallites on the order of 30−40 nm in size (Figure S5). The LITV-deposited materials had thicknesses of 8−12 μm with line widths of 30−40 μm (Figure 2a−c, left) as determined by optical profilometry. Depending on the specific oxide, a range of hierarchical, porous nano-morphologies were observed by scanning electron microscopy (Figure 2a−c, right), consistent with previous results.[37,38]

After integration of metal oxide semiconductor materials onto electrodes, a microheater was deposited. Most metal oxide semiconductor gas sensors incorporate the use of a heater to increase the otherwise sluggish adsorption/desorption kinetics for gaseous analytes on the metal oxide surface.[43] Accordingly, we fabricated a resistive heating pad from titanium to provide stable temperatures of up to 250 °C (see Experimental Section and Figures S1−S3). To test the stability of our sensing materials at these elevated temperatures, we ran stepwise heating of NiO, ramping the

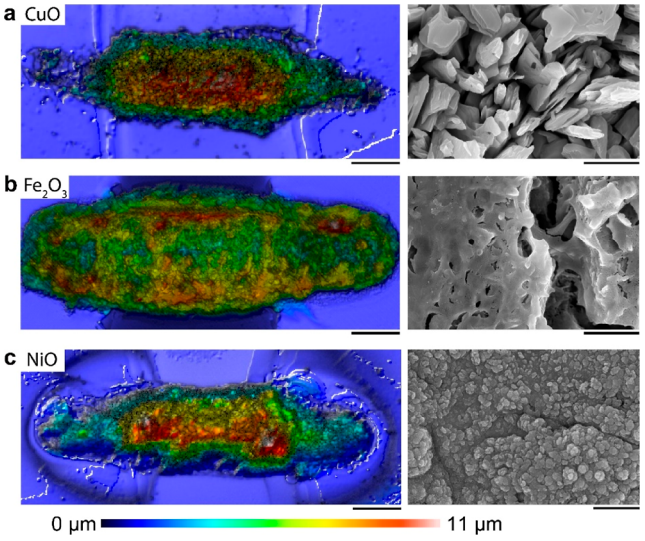

Figure 2. Morphological characterization of single-metal oxide materials. Optical profilometer images (left column) and scanning electron microscope images (right column) of the (a) CuO, (b) NiO, and (c) Fe_2O_3 sensors. Optical profilometry shows line widths of 30 to 50 μm and thicknesses of approximately 8 μm for NiO and CuO and 11 μm for Fe_2O_3. Scanning electron microscope images show microstructural variation between each material. Although all three materials were deposited using the same laser parameters, each has a different surface morphology with a hierarchy spanning the nano to microscale. Scale bars 20 μm (left) and 1 μm (right).

https://doi.org/10.1021/acsami.2c03561
ACS Appl. Mater. Interfaces 2022, 14, 28163−28173

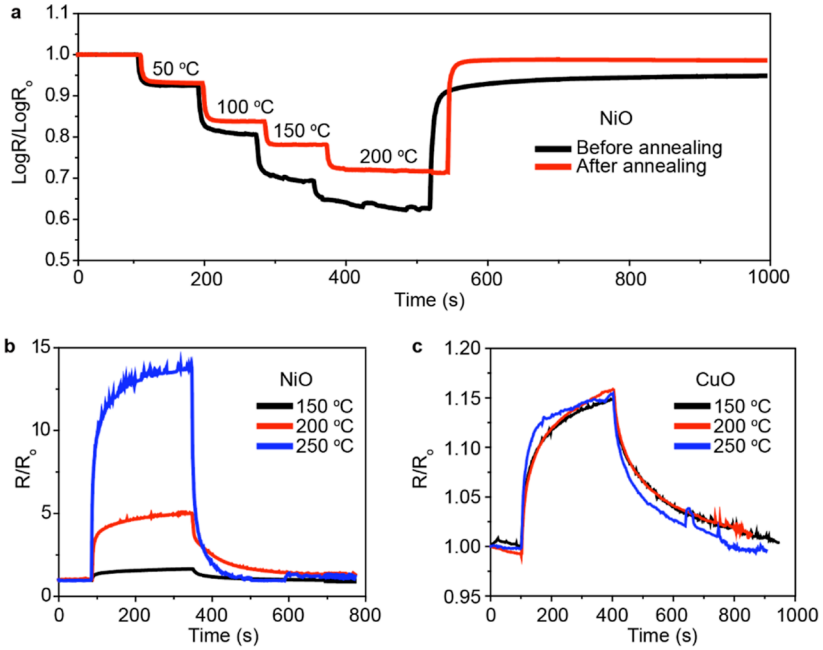

Figure 3. Temperature-dependent response of NiO and CuO sensors. (a) Effect of annealing on the stability of NiO baseline resistance revealed by the logarithmic ratio of baseline resistance to resistance at a given temperature $[\log(R/R_0)]$ vs time. Baseline sensor stability was tested by measuring NiO sensor resistance under stepwise increases in heater temperature. Unannealed samples show a more considerable resistance change with each temperature increase but fail to recover the original baseline resistance upon returning to room temperature (black line). This baseline drift was remedied by annealing for 24 h at 300 °C in the air, leading to decreased resistance dependence on temperature and a 97% recovery of the initial room temperature baseline (red line). (b) Temperature-dependent response of annealed NiO to 200 ppm ethanol. Higher temperatures lead to significantly improved sensing response. We find a peak response factor (R/R_0) of 13.9 at 250 °C. (c) Temperature-dependent response of annealed CuO to 200 ppm ethanol. No significant temperature dependence was observed over the temperature range. All tests were performed at 22% RH.

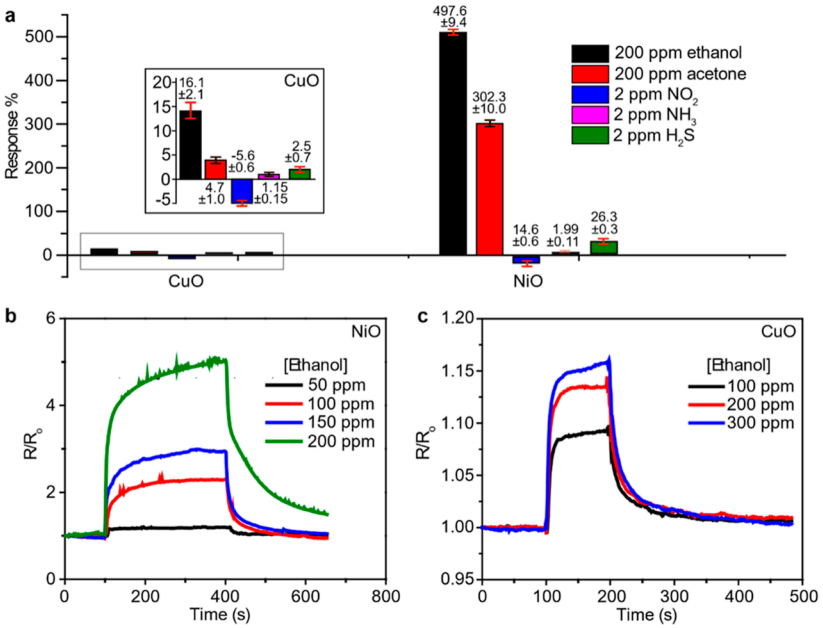

Figure 4. Response of single-metal oxide sensors to analyte gases. (a) Percentage response $[(R - R_0)/R_0*100]$ of CuO and NiO to 200 ppm ethanol and acetone, and 2 ppm NO_2, NH_3, and H_2S at 250 °C, with enlarged inset of CuO percent response for clarity. Both oxides show the largest response to ethanol and a minimal response to NH_3. Error bars were calculated based on the minimum and maximum response from three individual tests. The response of (b) NiO and (c) CuO to varying concentrations of ethanol vapor was measured at 250 °C. The results were used to calculate the theoretical limit of detection (LOD) for NiO and CuO. All tests were performed at 24% RH.

temperature in 50° increments from 50 to 200 °C, and measured the change in resistance (Figure 3a). While the resistance of the NiO decreased with the increasing temperature as expected, the material failed to recover to its initial room-temperature resistance upon cooling, which is undesirable (Figure 3a). We suspected that this drift in the baseline

https://doi.org/10.1021/acsami.2c03561
ACS Appl. Mater. Interfaces 2022, 14, 28163−28173

resistance might be due to partial annealing caused by the heater, as annealing of nanocrystalline materials has been shown to increase conductivity due to grain growth and defect closing even at relatively low temperatures.[44] To remedy this baseline drift, we pre-annealed the NiO samples in the air at 300 °C for 24 h in a furnace prior to device testing. Stability measurements on these pre-annealed samples showed a reduced degree of resistance change in response to heater temperature, reaching 97% of the original room temperature resistance after temperature cycling (Figure 3a).

Using these annealed NiO samples, we next investigated their resistive response to ethanol as a function of heater temperature. The gas sensors were heated to specific temperatures (150, 200, and 250 °C) for 30 min to stabilize the resistance before transferring the sample to a customized gas sensor testing chamber. The sensors were then exposed to 200 ppm ethanol for 5 min and moved to an ambient air environment for less than 10 min. The NiO exhibited increasing resistive response with higher temperatures, which is consistent with previous reports of NiO gas sensors (R/R_0 rose from 1.66 to 13.85, where R and R_0 are the resistance in the target gas and the air, respectively) (Figure 3b).[45,46] The same temperature-dependent ethanol response study was next carried out for annealed CuO sensors. Less temperature dependence was observed when exposed to ethanol over a temperature range from 150 to 250 °C (R/R_0 of CuO was 1.149, 1.158, and 1.144 for working temperatures of 150, 200, and 250 °C, respectively) (Figure 3c). This temperature-independent response to ethanol is inconsistent with other reported CuO gas sensors.[47,48] Metal oxide gas sensors most often show a sensitivity peak in the 250−400 °C range, with sensitivity decreasing at higher or lower temperatures. This effect has been attributed to the interplay between gas adsorption and desorption kinetics. As the temperature increases, the adsorption rate increases faster than the desorption rate, leading to increased sensitivity. At high temperatures, however, this relationship is flipped, with faster desorption rates leading to lower sensitivities.[6] The temperature-independent response of LITV-CuO could therefore indicate that the rates of adsorption and desorption are either minimally affected by temperature or increase at the same speed, resulting in no net change to sensitivity. Further study of this effect is outside the scope of this paper, but could yield insight into the fabrication of temperature-stable sensors. Fe_2O_3 was also tested in the same manner, but it showed high and unstable resistance values at all temperatures which did not resolve upon annealing at 300 °C, making pure LITV-Fe_2O_3 unsuitable for gas-sensing applications. As a result, all subsequent data for CuO, NiO, and mixed oxides described subsequently were collected at 250 °C using samples annealed at 300 °C for 24 h.

2.2. Selectivity Characterization of Sensor Response. We tested the response of CuO and NiO to a range of oxidizing and reducing gases, with results compiled in Figure 4. We found that both NiO and CuO exhibited the largest response to ethanol gas, with some sensitivity to acetone, NO_2, and H_2S but little response to NH_3 (Figure 4a). The response from the sensors based on CuO and NiO remained stable over short-term (multiple cycles, Figure S6) and long-term (eight months, Figure S7) testing for high-fidelity practical applications. The mechanism behind the response of CuO and NiO, both p-type semiconductors, to the reducing gases ethanol, acetone, NH_3, and H_2S can be explained as a transfer of electrons from the analyte gas to the oxide surface.[49] Upon heating, elemental oxygen adsorbed to the oxide surface is dissociated into negatively charged oxygen ions by trapping electrons from the oxide's conduction band, resulting in a distribution of adsorbed oxygen species consisting of $O_{2(ads)}$, $O^-_{2(ads)}$, $O^-_{(ads)}$, and $O^{2-}_{(ads)}$.[50] These ions create a surface layer of positive holes (h^+). When the surface is exposed to reducing gases, the reducing gases can either interact directly with the oxide surface or interact with the surface-bound oxygen ions, releasing electrons back into the oxide's conduction band. Since the dominant charge carrier of p-type semiconductors are holes, the electrons introduced due to interaction with reducing gases would lower the number of charge carriers present in the oxide grains, thus increasing the measured resistance.[51] A representative reaction for O^- species is shown below for ethanol (eq 1) and acetone (eq 2)[52]

$$CH_3CH_2OH_{(gas)} + 6O^-_{ads} \rightarrow 2CO_2 + 3H_2O + 6e^- \quad (1)$$

$$CH_3COCH_{3(gas)} + 8O^-_{ads} \rightarrow 3CO_2 + 3H_2O + 8e^- \quad (2)$$

Sensitivity to oxidizing gases follows a similar route, except that interaction with oxidizing gases results in the withdrawal of electrons from the oxide's conduction band, leading to an increased number of holes and a reduction in resistance.[49]

The theoretical limit of detection (LOD) for the NiO and CuO gas sensors was determined by testing the sensor's response to various ethanol concentrations at 250 °C. The responses of the NiO gas sensor to 50, 100, 150, and 200 ppm ethanol were 19.6, 129.4, 194.6, and 403.8%, respectively (Figure 4b), and the responses of the CuO gas sensor to 100, 200, and 300 ppm ethanol were 9.2, 13.0, and 15.9%, respectively (Figure 4c). The theoretical LOD was calculated for each oxide using the equation:[53] $LOD = 3 \times RMS_{noise}/slope$, yielding a theoretical estimation of ethanol LOD of 131.2 and 26.7 ppb for CuO and NiO, respectively. To experimentally verify these results, we exposed CuO and NiO to increasingly lower concentrations of ethanol (300 to 50 ppb for CuO (Figure S8) and 30 to 10 ppb for NiO (Figure S9). The minimum measurable concentration of ethanol was 100 ppb for CuO and 10 ppb for NiO with responses of 0.4% for CuO and 0.9% for NiO, respectively, both of which are slightly better than the predicted LOD from experiments at higher concentrations. Compared to other reported nanostructured CuO, we find that the sensitivity of LITV-CuO to ethanol is relatively low, with a 15.9% change at 300 ppm in this work and 60−230% change to 500 ppm ethanol in other works.[47,48,54−56] LITV-NiO shows competitive sensitivity to other reported nanostructured NiO such as NiO nanoplates[57] and hollow NiO hemispheres,[58] exhibiting sensitivities of 68.1% and 400% toward 200 ppm ethanol, respectively. We have compiled a table (Table S1) of selected metal oxide gas sensors to further show the competitive response of sensors fabricated using LITV.

2.3. Fabrication and Characterization of Mixed Metal Oxide Sensors. The strategic combination of various types of metal oxides to form metal−oxide/metal−oxide heterostructures has been shown to improve the selectivity and performance of gas sensors compared to single-metal oxide materials.[24] In addition, the doping of metal oxides with noble metals is also an effective way to enhance selectivity and sensitivity.[59] One of the most exciting aspects of LITV for gas sensor fabrication is the ability to combine multiple elements

https://doi.org/10.1021/acsami.2c03561
ACS Appl. Mater. Interfaces 2022, 14, 28163−28173

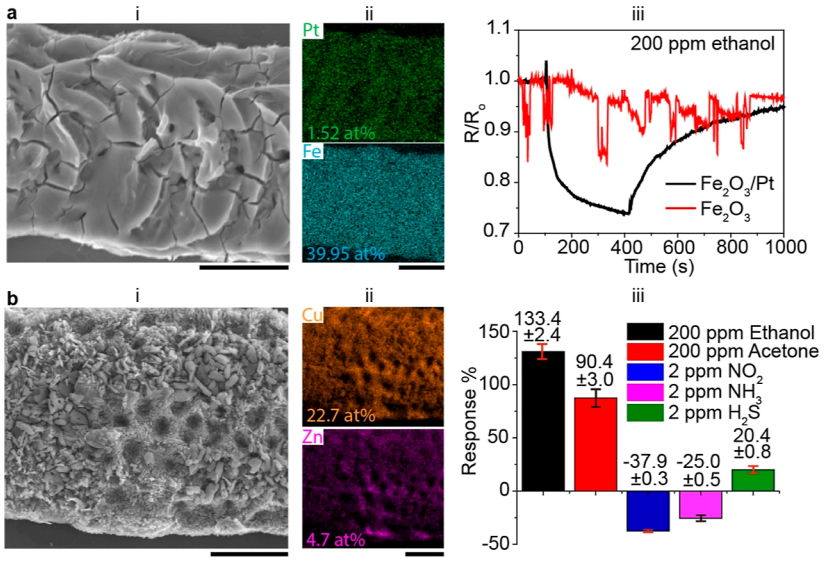

Figure 5. Characterization of morphology and gas response for mixed material sensors. (a) Scanning electron microscope and energy dispersive X-ray spectroscopy images showing (i) surface morphology and (ii) elemental distribution of Pt-doped Fe_2O_3. The sample shows a homogeneous distribution of Fe and Pt throughout the deposition. Elemental analysis shows a 25:1 at. % Fe/Pt ratio from the 20:1 M Fe/Pt salt ratio in the precursor solution. (iii) The addition of Pt into the Fe_2O_3 matrix creates a material with a measurable response to 200 ppm ethanol, an improvement from the pure Fe_2O_3, which shows no response. (b) Scanning electron microscope and energy dispersive X-ray spectroscopy images showing (i) surface morphology and (ii) elemental distribution for a 1:1:0.002 M $Cu(NO_3)_2/Zn(NO_3)_2/SnCl_4$ salt precursor. (iii) Percentage response $[(R - R_0)/R_0*100]$ of CuO/ZnO mixture to 200 ppm ethanol and acetone, and 2 ppm NO_2, NH_3, and H_2S at 250 °C. Error bars were calculated based on the minimum and maximum response from three individual tests. Elemental analysis shows that unlike the Fe/Pt sample, Cu and Zn are distributed inhomogeneously, and Cu is present in a 5:1 at. % ratio compared to Zn, suggesting preferential deposition of Cu over Zn from the precursor solution. This higher Cu concentration can help explain why the sample behaves primarily as a p-type semiconductor. Scale: 10 μm. All tests were performed at 24% RH.

into a single deposition by simply creating mixtures of the respective metal salts in the precursor solution.[37] To investigate this aspect of LITV in mixed-material gas sensor fabrication, we created two mixed materials: a Pt-doped Fe_2O_3 in 25:1 Fe/Pt at. % ratio and a 5:1 at. % ratio CuO/ZnO mixed oxide. The Pt-doped Fe_2O_3 sensor was chosen to investigate low-concentration doping of more reactive metal nanoparticles in a metal oxide semiconductor matrix and their subsequent gas-sensing behavior. We chose this system due to the failure of pure Fe_2O_3 to respond to any gas and its unstable resistance, aiming to create a material that would respond to gaseous analytes, where its single-oxide counterpart did not. The CuO/ZnO mixed oxide was chosen as a representative p−n heterojunction material, which we hypothesized could lead to better performance than the CuO alone.

The heterogeneous materials were prepared in the same general manner as the single oxides. The precursor solutions used were a 20:1 molar ratio of $Fe(NO_3)_3/(NH_4)_2PtCl_4$ and 1:1:0.002 molar ratio of $Cu(NO_3)_2/Zn(NO_3)_2/SnCl_4$ to deposit Fe_2O_3/Pt and CuO/ZnO, respectively. $SnCl_4$ was included after experimental observation that it promoted adhesion of the CuO/ZnO mixture to the glass substrate. We see no evidence of SnO_x species in any elemental or structural analysis (X-ray diffraction, X-ray photoelectron spectroscopy, energy dispersive X-ray spectroscopy, and transmission electron microscopy). Analysis of the deposited materials with scanning electron microscopy and energy dispersive X-ray spectroscopy as well as high resolution transmission electron microscopy (HRTEM) shows homogeneous Pt inclusion into the Fe_2O_3 with a slight preferential deposition of Fe over platinum at a ∼25:1 Fe/Pt at. % ratio (Figure 5ai,ii). HRTEM with energy dispersive X-ray spectroscopy shows small polycrystalline Pt and Fe_2O_3 grain sizes of <10−40 nm, with Pt metal grains interspersed in a matrix of crystalline α-Fe_2O_3 and amorphous iron oxide (Figure S10a). However, for the CuO/ZnO mixture, energy dispersive X-ray spectroscopy in a scanning electron microscope reveals inhomogeneous inclusion of ZnO into a CuO structure in a ∼5:1 Cu/Zn at. % ratio (Figure 5bi,ii), which suggests preferential deposition of CuO over ZnO from the precursor solution. HRTEM with energy dispersive X-ray spectroscopy also shows segregation of the CuO and ZnO grains, with 50−100 nm domains of the two separate oxides (Figure S10b). X-ray diffraction of the Fe_2O_3/Pt and CuO/ZnO materials confirms the structures of Fe_2O_3 with platinum metal inclusion and separate CuO and ZnO phases (Figure S11). High resolution X-ray photoelectron spectroscopy of the Zn, Cu, and Fe 2p core spectra can be best fitted using Zn with a 2+ valence, Cu with a mixture of 1+ and 2+ valence, and Fe with a mixture of 2+ and 3+ valence, while the Pt 4f core spectra can be best fitted using a mixture of 0, 2+, and 4+ valence (Figure S12). We note that these elemental valences are not strictly consistent with X-ray diffraction data, where we see only copper (II) oxide, iron (III) oxide, and metallic platinum. Previous X-ray photoelectron studies of Cu 2+ have reported that Cu 2+ can be reduced to Cu 1+ when exposed to high energy X-rays under ultra-high vacuum conditions, suggesting that the presence of Cu 1+ in our samples may be an instrumental artifact.[60] Platinum has also been shown to surface oxidize when in ambient conditions.[61] Since X-ray photoelectron spectroscopy is highly surface sensitive, the presence of 2+ and 4+ Pt peaks could be attributed to small amounts of surface oxidation. [104] α-Fe_2O_3 peaks in X-ray diffraction and HRTEM overlap with [311] peaks of Fe_3O_4, suggesting that divalent Fe may be

https://doi.org/10.1021/acsami.2c03561
ACS Appl. Mater. Interfaces 2022, 14, 28163−28173

present in these samples. While we do not see Fe_3O_4 peaks in X-ray diffraction, the signal-to-noise ratio is quite low, suggesting that smaller peaks may be hidden behind background signal.

The inclusion of Pt into the Fe_2O_3 matrix led to a decrease in material resistance, an increase in baseline stability, as well as a measurable response to 200 ppm ethanol gas of −26.2% (Figure 5aiii), which represents a significant improvement compared to Fe_2O_3 alone. Enhanced sensitivity of Pt-doped Fe_2O_3 to volatile organics such as ethanol and acetone was previously reported, with researchers suggesting the synergistic effect to be the cause of enhancement.[62] The synergistic effect is described as charge transfer from Fe_2O_3 to Pt due to Pt's higher work function, inducing an extension of the charge depletion layer at the surface of Fe_2O_3 further into the bulk. In addition, other researchers hypothesize that the existence of potential p-type PtO_x can form p−n junctions with n-type Fe_2O_3, contributing to the extension of the depletion layer, thus further modulating the sensor resistance and enhancing sensitivity.[62] Though the addition of Pt successfully improved the performance of Fe_2O_3 sensors fabricated by LITV, the sensitivity was still lower than other reports of Pt-doped Fe_2O_3.[62] This study demonstrated the ability to incorporate small amounts of metal additives that enhance sensor function, suggesting that further exploration of metal dopants into metal oxide structures using LITV could yield more sensitive materials in the future.

The mixed CuO/ZnO was used to examine the creation of semiconductor heterojunction materials and their sensing behavior using LITV. CuO/ZnO heterojunctions synthesized *via* various methods such as hydrothermal and photochemical have been previously reported to enhance sensitivity to a variety of gases, including H_2S and ethanol.[63,64] The CuO/ZnO gas sensors in this work were exposed to the target gas species for 200 s, followed by 900 s recovery at 250 °C, with % response for ethanol, acetone, NO_2, NH_3, and H_2S reported in Figure 5. Most notably, we find a marked increase in sensitivity to all gases measured, such as a 10-fold increase to ethanol and H_2S, a 20-fold increase to acetone, a 7-fold increase to NO_2, and a complete change in response character from p-type to n-type to NH_3 (Figure 5biii). An experimental measurement of the limit of detection resulted in a repeatable and measurable response to 2 ppb ethanol (Figure S13). When compared to pure CuO's limit of detection of 100 ppb toward ethanol, this result further supports the use of LITV to create mixed-oxide gas sensors. The response of pure CuO to 2 ppm NH_3 is minimal (Figure 4a), with only a 1% observed increase in resistance, but the response of CuO/ZnO to the same NH_3 concentration was found to be −25.5%. The minimal response of pure CuO to NH_3 may be overshadowed by a strong ZnO response, resulting in the observed change from a p-type to an n-type character for NH_3. Further study of the cause of this response could help guide more tailored material fabrication for targeting specific gases. The change from p-type to n-type response to NH_3 for this CuO/ZnO material could also be used as an indicator of analyte identity when characterizing mixed gas systems containing NH_3, making it a promising candidate for use in combinatorial sensing.

3. CONCLUSIONS

The LITV method was used to create microscale metal oxide gas sensors for the first time. The customizability of this direct laser writing platform was used to fabricate a variety of single oxides (CuO, NiO, Fe_2O_3), mixed oxides (CuO/ZnO), and metal-doped oxides (Fe_2O_3/Pt), demonstrating response to a variety of gases, including ethanol, acetone, NO_2, NH_3, and H_2S. We found significant enhancement of a 5 to 20-fold increase in response factor to all measured gases for the mixed CuO/ZnO system over that of pure CuO, which supports other reports in the literature that the creation of mixed oxide systems can lead to significant increases in sensor response and demonstrates the efficacy of LITV toward mixed-oxide gas sensor fabrication. The compositional and spatial control inherent to LITV, as well as the results reported herein, suggest that LITV is a promising candidate for the study and processing of microscale single- and mixed-oxide gas-sensing materials. We believe that this technique could be beneficial in high-throughput screening of mixed oxide structures or as a micropatterning technique for use in devices where more conventional drop-casting techniques are prohibitive to device fabrication. The microscale compositional and patterning control of LITV makes it an excellent candidate for the fabrication of high-density arrays of sensors necessary for combinatorial sensing. We hope that future studies will expand the materials and substrates compatible with LITV by investigating the use of flexible, polymeric substrates and further investigating the relationship between LITV processing parameters and subsequent material properties.

4. EXPERIMENTAL PROCEDURES

4.1. Materials. *4.1.1. Chemicals.* Metal salts $Cu(NO_3)_2{\cdot}3H_2O$ (Arcos Organics, 99%), $Ni(NO_3)_2{\cdot}6H_2O$ (Alfa Aesar, 98%), $Fe(NO_3)_3{\cdot}9H_2O$ (Alfa Aesar, 98%), $(NH_4)_2PtCl_4$ (Alfa Aesar, 99.9%+ metals basis), $SnCl_4{\cdot}5H_2O$ (Alfa Aesar, 98%), and $Zn(NO_3)_2{\cdot}6H_2O$ (Fisher Scientific, 99%) were used to create precursor solutions for LITV without any additional purification. Precursor solutions were made by dissolving 1 mmol (or 0.5 mmol for platinum precursor) of salt in 1 g of DI water, resulting in solutions of 19.4 wt % $Cu(NO_3)_2$, 22.8 wt % Zn (NO_3), 28.7 wt % $Fe(NO_3)_3$, 22.5 wt % $Ni(NO_3)_2$, 25.9 wt % $SnCl_4$, and 15.7 wt % $(NH_4)_2PtCl_4$. NO_2, H_2S, and NH_3 gases were prepared by diluting a standard calibration gas (116ES-112-25 GASCO Precision NO_2 calibration gas, 116ES-99-20 GASCO Precision H_2S calibration gas, and 116ES-14-10 GASCO precision NH_3 calibration gas) to the desired concentration with dry air. Acetone and ethanol were prepared by evaporation of acetone and ethanol droplets in the sealed gas chamber.

4.2. Methods. *4.2.1. Fabrication of Sensing Device.* Electron-beam evaporation (Temescal E-beam evaporator, Ferrotec Corporation) was used to deposit electrodes consisting of 10 nm Cr followed by 100 nm Au on glass coverslips (no. 1.5 Sigma-Aldrich) by employing a shadow mask. Electrode materials were chosen through trial and error based on the observed stability of the electrical contact between electrode pairs and the LITV-printed metal oxide. Electrode fingers were 100 μm wide with an 80 μm gap between electrodes in a pair and 400 μm between electrode pairs. Following electrode deposition, LITV was used to bridge the electrode gap to complete the circuit, using procedures described previously.[37,38] The LITV setup consists of a 780 nm continuous wave laser (Coherent MIRA 900F) with a motorized 1/2 wave plate/polarizing lens combination for power control, a set of galvanometer mirrors for beam rastering, and a nanoprecision microscope stage (Applied Scientific Instrumentation Modular Infinity Microscope) equipped with a 40× NA 0.6 objective (Nikon) as the focusing optic (Figure S14). The beam was expanded to fill the back aperture of the microscope objective using a set of convex lenses (Thorlabs N-BK7−B, f = 50 mm, and f = 100 mm) prior to the microscope stage. To bridge the electrodes with sensing material, 20 μL of the desired precursor solution was pipetted onto the electrodes [$Cu(NO_3)_2$ for CuO, $Ni(NO_3)_2$ for NiO, $Fe(NO_3)_3$ for Fe_2O_3, 1:1:0.002 molar ratio $Cu(NO_3)_2$/$Zn(NO_3)_2$/$SnCl_4$ for CuO/ZnO, and 20:1 molar ratio $Fe(NO_3)_3$/$(NH_4)_2PtCl_4$

https://doi.org/10.1021/acsami.2c03561
ACS Appl. Mater. Interfaces 2022, 14, 28163−28173

for Fe_2O_3/Pt]. The laser was rastered between the electrodes using the galvanometer mirrors at a rate of 5 pass/s with 250 mW power (measured after the objective) and allowed to scan for 10 s to create each sensor, leading to deposition of ∼30−40 μm wide lines of metal oxide bridging each electrode pair. To exchange the precursor, the sample was rinsed with DI water and then blown dry, followed by addition of 20 μL of the next precursor. After deposition of the metal oxide, the samples were annealed in a tube furnace (Lindberg/Blue 3-zone with a Eurotherm 3204 controller) under air at 300 °C for 24 h. Following this, 100 nm thick titanium heaters were printed onto the opposite side of the glass coverslip using sputtering with a polyimide shadow mask (Quorum Sputter Coater Q150R, see Figures S1−S3) to complete the fabrication process. We note that, while we did not carry out an in-depth study of laser-induced degradation of the electrodes, we find that we can consistently and reliably create stable and working circuits using LITV, suggesting that any electrode degradation is minimal and inconsequential.

4.2.2. Testing of Sensor Response. Gas sensor testing was carried out using a custom-built gas sensor test platform consisting of a 10 L glass chamber, a sample holder integrated onto the lid of the glass chamber, a source meter (Keithley 2401), and a laptop. For single gas sensors, the electrodes were wired out through the gas chamber lid to the source meter directly. For gas sensor array testing, a 16-channel relay module (Sainsmart) and a microcontroller (Arduino Uno) were added to the sample holder to enable sequential probing of each sensor. In all tests, the heater was turned on for at least 30 min before testing to achieve a stable resistance reading of the metal oxides. The target gas diluted to specific concentrations was injected into the gas chamber through a plastic syringe. After allowing the sensor to respond to the target gas in the chamber, the sensor was removed to recover in ambient air to finish the detection process.

4.2.3. Heater Design. A 3D finite element analysis of the steady temperature field of the gas sensor was studied for two different heater designs. The size of the glass coverslips is 18 mm × 20 mm with a thickness of 0.17 mm. The heater material was 100 nm titanium, and the electrode material was 10 nm chromium and 100 nm gold, consistent with the experiments. Based on the product datasheet, the density and thermal conductivity of the borosilicate glass coverslips (Corning) are 2.23 g/cm^3 and 1.14 W/m*K, respectively. The electrical conductivity of titanium is 6733.9 S/cm based on experimental data (Figure S1), which is lower than the value of bulk titanium (2.6×10^6 S/m). All other materials' properties are chosen directly from the COMSOL material library. Multiphysics module of the electric current and the heat transfer in solids is introduced in the COMSOL. The current density of the heater is calculated in the electric current module following Ohms law

$$\boldsymbol{J} = \sigma E \tag{3}$$

$$\boldsymbol{E} = -\nabla V \tag{4}$$

where J is the current density, σ is the electric conductivity, E is the electric field, and V is the electric potential. The two square electrode pads are set as ground and voltage terminals with different input voltage values. The temperature distribution of the entire gas sensor device is computed using the heat transfer in the solids module. The power generated from Joule heating is treated as heat flux Q_e according to

$$\rho C_p \mu \nabla T = \nabla \cdot (k \nabla T) + Q_e \tag{5}$$

$$Q_e = \boldsymbol{J} \cdot \boldsymbol{E} \tag{6}$$

where ρ is the density, C_p is the heat capacity at constant pressure, k is the thermal conductivity, and T is the temperature. All air-exposed surfaces are treated as heat convection boundaries, and the boundary condition is added as

$$q_o = h \cdot (T_{ext} - T) \tag{7}$$

Here, q_0 is the convective heat flux, T_{ext} is the room temperature at 293.15 K, and h is the heat transfer coefficient. For free convection of static air, h ranges from 5 to 25 W/m^2/K in natural conditions.[65] Based on the agreement between experimental and simulation results, we find a value of 12 W/m^2/K to be the most representative for this sensor design.

Initially, an "I" shape heater patterned on the same side of the electrodes (frontside) was examined (Figure S2ai). However, the temperature distribution was not uniform along the heater direction (the center has a 12% higher temperature than the edge), and a steep drop off temperature was observed from the heater to the electrodes (from 250 to 142 °C). The temperature drop can also cause a crack failure of the glass coverslips due to the thermal stress induced by uneven heating. To ensure a more uniform heat distribution and prevent device failure, a 7 mm × 6 mm heater patterned on the backside of the glass with the heating region overlapping the electrodes was used to replace the "I" shape heater (Figure S2aii). Compared with the "I" shaped heater on the front side, the COMSOL simulation shows that the backside heater generates a more uniform temperature distribution (a 4% temperature difference between the central electrode and the edge electrode) at the electrode area. Therefore, the backside heater was adopted to collect all sensor response data. The correlation between temperature (both experimental and COMSOL simulation) and applied voltage is shown in Figure S2b for the two types of heaters. We found that the backside heater exhibited stable temperature variation up to 250 °C (Figure S2bii), requiring 0.040 mA at 30 V to reach 250 °C.

4.2.4. Heater Thermal Characterization. A thermal camera (FLIR One pro) was used to verify the operating temperature of the gas sensor before testing (Figure S2b). The key specifications of the thermal camera include focus distance of 15 cm, frame rate of 8.7 Hz, thermal sensitivity of 70 mK, and sensor pixel size of 8−14 μm.

4.3. Characterization of Sensing Materials. *4.3.1. Scanning Electron Microscopy and Energy Dispersive X-Ray Spectroscopy.* Field emission scanning electron microscopy (Verios G4) equipped with energy-dispersive X-ray spectroscopy was conducted using instrumentation at the Materials Characterization Laboratory at The Pennsylvania State University. Scanning electron microscope images were taken under various beam currents (30−100 pA) and landing energies (5−10 keV) to optimize image quality. Energy-dispersive X-ray spectroscopy was done at 20 keV and 1.2 nA after beam calibration using copper tape as a reference signal, and analysis was done using Aztec software (Oxford Instruments). Samples were not polished, resulting in approximately 2−3% error of the resulting compositional analysis due to scattering and reabsorption of characteristic emission from the rough sample surface.

4.3.2. Profilometry. Profilometry was conducted using an optical profilometer (Sensofar S Lynx). Images were taken in confocal mode using a 100× objective, and missing data points were interpolated using the profilometer software (SensoVIEW), which uses an average of neighboring heights to approximate the missing pixel. All profilometry images used had >96% initial data collection.

4.3.3. X-Ray Diffraction. X-ray diffraction (Malvern Panalytical Empyrean II for Co source and Malvern Panalytical X'Pert Pro MPD for Cu source, both with an X'celerator detector) was conducted at the Materials Characterization Laboratory at The Pennsylvania State University. Scans were run using a Co and Cu line source (Co Kα λ = 1.79026 Å and Cu Kα radiation, λ = 1.54184 Å) with 0.02° step sizes at 150 s/step. Samples analyzed were 1.2 × 1 mm rectangles deposited on glass coverslips with the same LITV technique used for gas sensor fabrication. Analysis of the resulting patterns was done using JADE software.

4.3.4. X-Ray Photoelectron Spectroscopy. X-ray photoelectron spectroscopy measurements were performed using Physical Electronics PHI VersaProbe III equipped with a concentric hemispherical analyzer. Before measurement, samples were loaded into the intro chamber and pumped to pressures of ∼10^{-10} Torr. Samples were then transferred to the main chamber and irradiated using a monochromatic Al Kα X-ray source (15 kV, ∼48 W) over a spot size of 200 μm. The survey and high-resolution spectra were recorded with pass energies of 280 and 112 eV, respectively. Charge neutralizers were used during all acquisitions using both low energy electrons (<5 eV) and argon ions. A takeoff angle of 45° with respect to the sample

https://doi.org/10.1021/acsami.2c03561
ACS Appl. Mater. Interfaces 2022, 14, 28163−28173

surface plane was used for measurements. Typical sampling depths of 3−6 nm (95% of the signal originated from this depth or shallower) were obtained from this. Quantification was done using instrumental relative sensitivity factors (RSFs) that account for the X-ray cross section and inelastic mean free path of the electrons. All survey spectra were charge referenced with respect to the adventitious carbon peak at 284.8 eV. Data were analyzed using CasaXPS Version 2.3.23.PR1.0.45. All peaks were fitted using an Iterated Shirley background subtraction using an asymmetric Lorentzian lineshape LA (1.53, 243). Relative error was calculated using Monte Carlo error analyses in CasaXPS. All fittings were carried out with reference to binding energy and full width at half maximum (FWHM) values obtained from databases and relevant literature.[60,66−68]

4.3.5. High Resolution Transmission Electron Microscopy and Energy Dispersive Spectroscopy. Particles of the laser-deposited samples were scratched off the surface of the glass substrate, dispersed in ethanol, and ultrasonicated for 5 min. The particle dispersion was then drop-cast onto lacey carbon TEM grids. HRTEM and scanning TEM/EDS (STEM-EDS) of the sample were performed using an FEI Talos F200X microscope at The Pennsylvania State University, operating at an accelerating voltage of 200 kV and offering angstrom image resolution. A high angle annular dark field detector was used for STEM image acquisition and EDS data collection using the Super-X EDS quad detector system at an accelerating voltage of 200 kV and a current of ∼0.15 nA. Standardless Cliff-Lorimer quantification was performed on the deconvoluted EDS line intensity data using the Bruker Espirit software.

■ ASSOCIATED CONTENT

Supporting Information

The Supporting Information is available free of charge at https://pubs.acs.org/doi/10.1021/acsami.2c03561.

> Heater characterization; electrode design; X-ray diffraction and Rietveld refinement; sensor stability measurements; limit of detection measurements; transmission electron microscopy and elemental analysis; X-ray photoelectron spectroscopy; laser table schematic; and comparative gas sensor response data (PDF)

■ AUTHOR INFORMATION

Corresponding Authors

Lauren D. Zarzar − *Department of Chemistry, The Pennsylvania State University, University Park, Pennsylvania 16802, United States; Department of Materials Science and Engineering and Materials Research Institute, The Pennsylvania State University, University Park, Pennsylvania 16802, United States;* orcid.org/0000-0002-3287-3602; Email: ldz4@psu.edu

Huanyu Cheng − *Department of Materials Science and Engineering, Department of Engineering Science and Mechanics, and Materials Research Institute, The Pennsylvania State University, University Park, Pennsylvania 16802, United States;* orcid.org/0000-0001-6075-4208; Email: huanyu.cheng@psu.edu

Authors

Alexander C. Castonguay − *Department of Chemistry, The Pennsylvania State University, University Park, Pennsylvania 16802, United States;* orcid.org/0000-0003-3081-9423

Ning Yi − *Department of Materials Science and Engineering, The Pennsylvania State University, University Park, Pennsylvania 16802, United States;* orcid.org/0000-0002-4116-5202

Bowen Li − *Department of Engineering Science and Mechanics, The Pennsylvania State University, University Park, Pennsylvania 16802, United States*

Jiang Zhao − *Department of Engineering Science and Mechanics, The Pennsylvania State University, University Park, Pennsylvania 16802, United States*

Han Li − *Department of Engineering Science and Mechanics, The Pennsylvania State University, University Park, Pennsylvania 16802, United States; Pen-Tung Sah Institute of Micro-Nano Science and Technology, Xiamen University, Xiamen 361005, China; Southeast Institute of China Unicom, Fuzhou 350000, China*

Yuyan Gao − *Department of Engineering Science and Mechanics, The Pennsylvania State University, University Park, Pennsylvania 16802, United States*

Nabila N. Nova − *Department of Chemistry, The Pennsylvania State University, University Park, Pennsylvania 16802, United States*

Naveen Tiwari − *Department of Engineering Science and Mechanics, The Pennsylvania State University, University Park, Pennsylvania 16802, United States;* orcid.org/0000-0002-4252-3235

Complete contact information is available at: https://pubs.acs.org/10.1021/acsami.2c03561

Author Contributions

[¶]A.C.C. and N.Y. contributed equally to this work

Notes

The authors declare no competing financial interest.

■ ACKNOWLEDGMENTS

AC and L.D.Z. acknowledge funding from the NSF (grant CMMI-2046819) and the Sloan Research Fellowship. H.C. acknowledges the support provided by NIH (award nos. R21EB030140, U01DA056242, and R61H.L.154215), NSF (grant no. ECCS-1933072), and Penn State University. A.C., L.D.Z., N.Y., and H.C. acknowledge funding from the Penn State Institutes of Energy and the Environment. B.L. acknowledges the Leighton Riess Graduate Fellowship in Engineering at Penn State University.

■ REFERENCES

(1) Kaushik, A.; Kumar, R.; Arya, S. K.; Nair, M.; Malhotra, B. D.; Bhansali, S. Organic-Inorganic Hybrid Nanocomposite-Based Gas Sensors for Environmental Monitoring. *Chem. Rev.* **2015**, *115*, 4571−4606.

(2) Hagleitner, C.; Hierlemann, A.; Lange, D.; Kummer, A.; Kerness, N.; Brand, O.; Baltes, H. Smart Single-Chip Gas Sensor Microsystem. *Nature* **2001**, *414*, 293−296.

(3) Shin, J.; Choi, S.-J.; Lee, I.; Youn, D.-Y.; Park, C. O.; Lee, J.-H.; Tuller, H. L.; Kim, I.-D. Thin-Wall Assembled SnO_2 Fibers Functionalized by Catalytic Pt Nanoparticles and Their Superior Exhaled-Breath-Sensing Properties for the Diagnosis of Diabetes. *Adv. Funct. Mater.* **2013**, *23*, 2357−2367.

(4) Mirica, K. A.; Azzarelli, J. M.; Weis, J. G.; Schnorr, J. M.; Swager, T. M. Rapid Prototyping of Carbon-Based Chemiresistive Gas Sensors on Paper. *Proc. Natl. Acad. Sci. U.S.A.* **2013**, *110*, E3265−E3270.

(5) Wan, Q.; Li, Q. H.; Chen, Y. J.; Wang, T. H.; He, X. L.; Li, J. P.; Lin, C. L. Fabrication and Ethanol Sensing Characteristics of ZnO Nanowire Gas Sensors. *Appl. Phys. Lett.* **2004**, *84*, 3654−3656.

(6) Kolmakov, A.; Klenov, D. O.; Lilach, Y.; Stemmer, S.; Moskovits, M. Enhanced Gas Sensing by Individual SnO_2 Nanowires and

Nanobelts Functionalized with Pd Catalyst Particles. *Nano Lett.* **2005**, *5*, 667−673.
(7) Li, H.; Xie, W.; Liu, B.; Wang, Y.; Xiao, S.; Duan, X.; Li, Q.; Wang, T. Ultra-Fast and Highly-Sensitive Gas Sensing Arising from Thin SnO_2 Inner Wall Supported Hierarchical Bilayer Oxide Hollow Spheres. *Sens. Actuators, B* **2017**, *240*, 349−357.
(8) Liu, X.; Cheng, S.; Liu, H.; Hu, S.; Zhang, D.; Ning, H. A Survey on Gas Sensing Technology. *Sensors* **2012**, *12*, 9635−9665.
(9) Li, H.; Xie, W.; Ye, T.; Liu, B.; Xiao, S.; Wang, C.; Wang, Y.; Li, Q.; Wang, T. Temperature-Dependent Abnormal and Tunable p-n Response of Tungsten Oxide-Tin Oxide Based Gas Sensors. *ACS Appl. Mater. Interfaces* **2015**, *7*, 24887−24894.
(10) Bai, S.; Li, D.; Han, D.; Luo, R.; Chen, A.; Chung, C. L. Preparation, Characterization of WO_3-SnO_2 Nanocomposites and Their Sensing Properties for NO_2. *Sens. Actuators, B* **2010**, *150*, 749−755.
(11) Katoch, A.; Kim, J.-H.; Kim, S. S. Significance of the Nanograin Size on the H_2S-Sensing Ability of CuO-SnO_2 Composite Nanofibers. *J. Sens.* **2015**, *2015*, 387641.
(12) Yin, M.; Yao, Y.; Fan, H.; Liu, S. WO_3-SnO_2 Nanosheet Composites: Hydrothermal Synthesis and Gas Sensing Mechanism. *J. Alloys Compd.* **2018**, *736*, 322−331.
(13) Trakhtenberg, L. I.; Gerasimov, G. N.; Gromov, V. F.; Belysheva, T. V.; Ilegbusi, O. J. Effect of Composition and Temperature on Conductive and Sensing Properties of CeO_2 + In_2O_3 Nanocomposite Films. *Sens. Actuators, B* **2015**, *209*, 562−569.
(14) Zhang, Y.-B.; Yin, J.; Li, L.; Zhang, L.-X.; Bie, L.-J. Enhanced Ethanol Gas-Sensing Properties of Flower-like p-CuO/n-ZnO Heterojunction Nanorods. *Sens. Actuators, B* **2014**, *202*, 500−507.
(15) Wang, C.; Cui, X.; Liu, J.; Zhou, X.; Cheng, X.; Sun, P.; Hu, X.; Li, X.; Zheng, J.; Lu, G. Design of Superior Ethanol Gas Sensor Based on Al-Doped NiO Nanorod-Flowers. *ACS Sens.* **2016**, *1*, 131−136.
(16) Hou, L.; Zhang, C.; Li, L.; Du, C.; Li, X.; Kang, X.-F.; Chen, W. CO Gas Sensors Based on p-Type CuO Nanotubes and CuO Nanocubes: Morphology and Surface Structure Effects on the Sensing Performance. *Talanta* **2018**, *188*, 41−49.
(17) Wan, X.; Wang, J.; Zhu, L.; Tang, J. Gas Sensing Properties of Cu_2O and Its Particle Size and Morphology-Dependent Gas-Detection Sensitivity. *J. Mater. Chem. A* **2014**, *2*, 13641−13647.
(18) Woo, H.-S.; Na, C. W.; Lee, J.-H. Design of Highly Selective Gas Sensors via Physicochemical Modification of Oxide Nanowires: Overview. *Sensors* **2016**, *16*, 1531.
(19) Siebert, L.; Lupan, O.; Mirabelli, M.; Ababii, N.; Terasa, M.-I.; Kaps, S.; Cretu, V.; Vahl, A.; Faupel, F.; Adelung, R. 3D-Printed Chemiresistive Sensor Array on Nanowire CuO/Cu_2O/Cu Heterojunction Nets. *ACS Appl. Mater. Interfaces* **2019**, *11*, 25508−25515.
(20) Patil, D.; Patil, L. Cr_2O_3-Modified ZnO Thick Film Resistors as LPG Sensors. *Talanta* **2009**, *77*, 1409−1414.
(21) Patil, D. R.; Patil, L. A.; Patil, P. P. Cr_2O_3-Activated ZnO Thick Film Resistors for Ammonia Gas Sensing Operable at Room Temperature. *Sens. Actuators, B* **2007**, *126*, 368−374.
(22) Nakate, U. T.; Ahmad, R.; Patil, P.; Wang, Y.; Bhat, K. S.; Mahmoudi, T.; Yu, Y. T.; Suh, E.-k.; Hahn, Y.-B. Improved Selectivity and Low Concentration Hydrogen Gas Sensor Application of Pd Sensitized Heterojunction n-ZnO/p-NiO Nanostructures. *J. Alloys Compd.* **2019**, *797*, 456−464.
(23) Miller, D. R.; Akbar, S. A.; Morris, P. A. Nanoscale Metal Oxide-Based Heterojunctions for Gas Sensing: A Review. *Sens. Actuators, B* **2014**, *204*, 250−272.
(24) Zappa, D.; Galstyan, V.; Kaur, N.; Munasinghe Arachchige, H. M. M.; Sisman, O.; Comini, E. "Metal Oxide-Based Heterostructures for Gas Sensors"-A Review. *Anal. Chim. Acta* **2018**, *1039*, 1−23.
(25) Dey, A. Semiconductor Metal Oxide Gas Sensors: A Review. *Mater. Sci. Eng., B* **2018**, *229*, 206−217.
(26) Tan, Y.; Li, C.; Wang, Y.; Tang, J.; Ouyang, X. Fast-Response and High Sensitivity Gas Sensors Based on SnO_2 Hollow Spheres. *Thin Solid Films* **2008**, *516*, 7840−7843.
(27) Martinez, C. J.; Hockey, B.; Montgomery, C. B.; Semancik, S. Porous Tin Oxide Nanostructured Microspheres for Sensor Applications. *Langmuir* **2005**, *21*, 7937−7944.
(28) Li, H.; Liu, B.; Cai, D.; Wang, Y.; Liu, Y.; Mei, L.; Wang, L.; Wang, D.; Li, Q.; Wang, T. High-Temperature Humidity Sensors Based on WO_3-SnO_2 Composite Hollow Nanospheres. *J. Mater. Chem. A* **2014**, *2*, 6854−6862.
(29) Dubourg, G.; Radović, M. Multifunctional Screen-Printed TiO_2 Nanoparticles Tuned by Laser Irradiation for a Flexible and Scalable UV Detector and Room-Temperature Ethanol Sensor. *ACS Appl. Mater. Interfaces* **2019**, *11*, 6257−6266.
(30) Barsan, N.; Koziej, D.; Weimar, U. Metal Oxide-Based Gas Sensor Research: How To? *Sens. Actuators, B* **2007**, *121*, 18−35.
(31) Armon, N.; Greenberg, E.; Edri, E.; Nagler-Avramovitz, O.; Elias, Y.; Shpaisman, H. Laser-Based Printing: From Liquids to Microstructures. *Adv. Funct. Mater.* **2021**, *31*, 2008547.
(32) Yeo, J.; Hong, S.; Kim, G.; Lee, H.; Suh, Y. D.; Park, I.; Grigoropoulos, C. P.; Ko, S. H. Laser-Induced Hydrothermal Growth of Heterogeneous Metal-Oxide Nanowire on Flexible Substrate by Laser Absorption Layer Design. *ACS Nano* **2015**, *9*, 6059−6068.
(33) Kong, H.; Kim, H.; Hwang, S.; Mun, J.; Yeo, J. Laser-Induced Hydrothermal Growth of Iron Oxide Nanoparticles on Diverse Substrates for Flexible Micro-supercapacitors. *ACS Appl. Nano Mater.* **2022**, *5*, 4102−4111.
(34) Yeo, J.; Hong, S.; Wanit, M.; Kang, H. W.; Lee, D.; Grigoropoulos, C. P.; Sung, H. J.; Ko, S. H. Rapid, One-Step, Digital Selective Growth of ZnO Nanowires on 3D Structures Using Laser Induced Hydrothermal Growth. *Adv. Funct. Mater.* **2013**, *23*, 3316−3323.
(35) Luo, S.; Hoang, P. T.; Liu, T. Direct Laser Writing for Creating Porous Graphitic Structures and Their Use for Flexible and Highly Sensitive Sensor and Sensor Arrays. *Carbon* **2016**, *96*, 522−531.
(36) Wu, D.; Peng, Q.; Wu, S.; Wang, G.; Deng, L.; Tai, H.; Wang, L.; Yang, Y.; Dong, L.; Zhao, Y.; Zhao, J.; Sun, D.; Lin, L. A Simple Graphene NH_3 Gas Sensor via Laser Direct Writing. *Sensors* **2018**, *18*, 4405.
(37) Kindle, C.; Castonguay, A.; McGee, S.; Tomko, J. A.; Hopkins, P. E.; Zarzar, L. D. Direct Laser Writing from Aqueous Precursors for Nano to Microscale Topographical Control, Integration, and Synthesis of Nanocrystalline Mixed Metal Oxides. *ACS Appl. Nano Mater.* **2019**, *2*, 2581−2586.
(38) Zarzar, L. D.; Swartzentruber, B. S.; Donovan, B. F.; Hopkins, P. E.; Kaehr, B. Using Laser-Induced Thermal Voxels to Pattern Diverse Materials at the Solid-Liquid Interface. *ACS Appl. Mater. Interfaces* **2016**, *8*, 21134−21139.
(39) Balaish, M.; Rupp, J. L. M. Widening the Range of Trackable Environmental and Health Pollutants for Li-Garnet-Based Sensors. *Adv. Mater.* **2021**, *33*, 2100314.
(40) Urriza-Arsuaga, I.; Bedoya, M.; Orellana, G. Tailored Luminescent Sensing of NH_3 in Biomethane Productions. *Sens. Actuators, B* **2019**, *292*, 210−216.
(41) Wilson, A. D. Applications of Electronic-Nose Technologies for Noninvasive Early Detection of Plant, Animal and Human Diseases. *Chemosensors* **2018**, *6*, 45.
(42) Cornforth, D. M.; Popat, R.; McNally, L.; Gurney, J.; Scott-Phillips, T. C.; Ivens, A.; Diggle, S. P.; Brown, S. P. Combinatorial Quorum Sensing Allows Bacteria to Resolve Their Social and Physical Environment. *Proc. Natl. Acad. Sci. U.S.A.* **2014**, *111*, 4280−4284.
(43) Miller, D. R.; Akbar, S. A.; Morris, P. A. Nanoscale Metal Oxide-Based Heterojunctions for Gas Sensing: A Review. *Sens. Actuators, B* **2014**, *204*, 250−272.
(44) Korotcenkov, G.; Cho, B. K. The Role of Grain Size on the Thermal Instability of Nanostructured Metal Oxides Used in Gas Sensor Applications and Approaches for Grain-Size Stabilization. *Prog. Cryst. Growth Charact. Mater.* **2012**, *58*, 167−208.
(45) Sun, X.; Hu, X.; Wang, Y.; Xiong, R.; Li, X.; Liu, J.; Ji, H.; Li, X.; Cai, S.; Zheng, C. Enhanced Gas-Sensing Performance of Fe-Doped Ordered Mesoporous NiO with Long-Range Periodicity. *J. Phys. Chem. C* **2015**, *119*, 3228−3237.

https://doi.org/10.1021/acsami.2c03561
ACS Appl. Mater. Interfaces 2022, 14, 28163−28173

(46) Miao, R.; Zeng, W.; Gao, Q. SDS-Assisted Hydrothermal Synthesis of NiO Flake-Flower Architectures with Enhanced Gas-Sensing Properties. *Appl. Surf. Sci.* **2016**, *384*, 304−310.
(47) Zhu, G.; Xu, H.; Xiao, Y.; Liu, Y.; Yuan, A.; Shen, X. Facile Fabrication and Enhanced Sensing Properties of Hierarchically Porous CuO Architectures. *ACS Appl. Mater. Interfaces* **2012**, *4*, 744−751.
(48) Han, C.; Chen, X.; Liu, D.; Zhou, P.; Zhao, S.; Bi, H.; Meng, D.; Wei, D.; Shen, Y. Fabrication of Shrub-like CuO Porous Films by a Top-down Method for High-Performance Ethanol Gas Sensor. *Vacuum* **2018**, *157*, 332−339.
(49) Fine, G. F.; Cavanagh, L. M.; Afonja, A.; Binions, R. Metal Oxide Semi-Conductor Gas Sensors in Environmental Monitoring. *Sensors* **2010**, *10*, 5469−5502.
(50) Bielański, A.; Najbar, M. Adsorption Species of Oxygen on the Surfaces of Transition Metal Oxides. *J. Catal.* **1972**, *25*, 398−406.
(51) Pargoletti, E.; Cappelletti, G. Breakthroughs in the Design of Novel Carbon-Based Metal Oxides Nanocomposites for VOCs Gas Sensing. *Nanomaterials* **2020**, *10*, 1485.
(52) Wang, J.; Yang, J.; Han, N.; Zhou, X.; Gong, S.; Yang, J.; Hu, P.; Chen, Y. Highly Sensitive and Selective Ethanol and Acetone Gas Sensors Based on Modified ZnO Nanomaterials. *Mater. Des.* **2017**, *121*, 69−76.
(53) Yang, L.; Yi, N.; Zhu, J.; Cheng, Z.; Yin, X.; Zhang, X.; Zhu, H.; Cheng, H. Novel Gas Sensing Platform Based on a Stretchable Laser-Induced Graphene Pattern with Self-Heating Capabilities. *J. Mater. Chem. A* **2020**, *8*, 6487−6500.
(54) Hien, V. X.; Minh, N. H.; Son, D. T.; Nghi, N. T.; Phuoc, L. H.; Khoa, C. T.; Vuong, D. D.; Chien, N. D.; Heo, Y.-W. Acetone Sensing Properties of CuO Nanowalls Synthesized via Oxidation of Cu Foil in Aqueous NH_4OH. *Vacuum* **2018**, *150*, 129−135.
(55) Wang, C.; Fu, X. Q.; Xue, X. Y.; Wang, Y. G.; Wang, T. H. Surface Accumulation Conduction Controlled Sensing Characteristic of p-Type CuO Nanorods Induced by Oxygen Adsorption. *Nanotechnology* **2007**, *18*, 145506.
(56) Gou, X.; Wang, G.; Yang, J.; Park, J.; Wexler, D. Chemical Synthesis, Characterisation and Gas Sensing Performance of Copper Oxide Nanoribbons. *J. Mater. Chem.* **2008**, *18*, 965−969.
(57) Su, C.; Zhang, L.; Han, Y.; Ren, C.; Chen, X.; Hu, J.; Zeng, M.; Hu, N.; Su, Y.; Zhou, Z.; Yang, Z. Controllable Synthesis of Crescent-Shaped Porous NiO Nanoplates for Conductometric Ethanol Gas Sensors. *Sens. Actuators, B* **2019**, *296*, 126642.
(58) Cho, N. G.; Hwang, I.-S.; Kim, H.-G.; Lee, J.-H.; Kim, I.-D. Gas Sensing Properties of P-Type Hollow NiO Hemispheres Prepared by Polymeric Colloidal Templating Method. *Sens. Actuators, B* **2011**, *155*, 366−371.
(59) Wang, C.; Yin, L.; Zhang, L.; Xiang, D.; Gao, R. Metal Oxide Gas Sensors: Sensitivity and Influencing Factors. *Sensors* **2010**, *10*, 2088−2106.
(60) Wu, C.-K.; Yin, M.; O'Brien, S.; Koberstein, J. T. Quantitative Analysis of Copper Oxide Nanoparticle Composition and Structure by X-Ray Photoelectron Spectroscopy. *Chem. Mater.* **2006**, *18*, 6054−6058.
(61) Parkinson, C. R.; Walker, M.; McConville, C. F. Reaction of Atomic Oxygen with a Pt(111) Surface: Chemical and Structural Determination Using XPS, CAICISS and LEED. *Surf. Sci.* **2003**, *545*, 19−33.
(62) Liu, C.; Gao, H.; Wang, L.; Wang, T.; Yang, X.; Sun, P.; Gao, Y.; Liang, X.; Liu, F.; Song, H.; Lu, G. Facile Synthesis and the Enhanced Sensing Properties of Pt-Loaded α-Fe_2O_3 Porous Nanospheres. *Sens. Actuators, B* **2017**, *252*, 1153−1162.
(63) Huang, J.; Dai, Y.; Gu, C.; Sun, Y.; Liu, J. Preparation of Porous Flower-like CuO/ZnO Nanostructures and Analysis of Their Gas-Sensing Property. *J. Alloys Compd.* **2013**, *575*, 115−122.
(64) Kim, J.; Kim, W.; Yong, K. CuO/ZnO Heterostructured Nanorods: Photochemical Synthesis and the Mechanism of H_2S Gas Sensing. *J. Phys. Chem. C* **2012**, *116*, 15682−15691.
(65) Convection Heat Coefficient. http://help.solidworks.com/2014/english/solidworks/cworks/c_convection_heat_coefficient.htm (accessed Jan 2, 2022).
(66) Yamashita, T.; Hayes, P. Analysis of XPS Spectra of Fe^{2+} and Fe^{3+} Ions in Oxide Materials. *Appl. Surf. Sci.* **2008**, *254*, 2441−2449.
(67) Mazzotta, E.; Rella, S.; Turco, A.; Malitesta, C. XPS in Development of Chemical Sensors. *RSC Adv.* **2015**, *5*, 83164−83186.
(68) Naumkin, A.; Kraut-Vass, A.; Gaarenstroom, S. W.; Powell, C. J. *NIST X-Ray Photoelectron Spectroscopy (XPS) Database*; version 3.5, 2022.(accessed Mar 2, 2022).